applied optics

Micro-optical design of a three-dimensional microlens scanner for vertically integrated micro-opto-electro-mechanical systems

Maciej Baranski,[1] Sylwester Bargiel,[1] Nicolas Passilly,[1,*] Christophe Gorecki,[1] Chenping Jia,[2] Jörg Frömel,[2] and Maik Wiemer[2]

[1]MN2S Department, FEMTO-ST Institute, University of Franche-Comté, CNRS (UMR6174) 15B Avenue des Montboucons, 25030 Besançon, France
[2]System Packaging Department, Fraunhofer Institute for Electronic Nanosystems, 09126 Chemnitz, Germany
*Corresponding author: nicolas.passilly@femto-st.fr

Received 15 May 2015; revised 29 June 2015; accepted 8 July 2015; posted 9 July 2015 (Doc. ID 241133); published 30 July 2015

This paper presents the optical design of a miniature 3D scanning system, which is fully compatible with the vertical integration technology of micro-opto-electro-mechanical systems (MOEMS). The constraints related to this integration strategy are considered, resulting in a simple three-element micro-optical setup based on an afocal scanning microlens doublet and a focusing microlens, which is tolerant to axial position inaccuracy. The 3D scanning is achieved by axial and lateral displacement of microlenses of the scanning doublet, realized by micro-electro-mechanical systems microactuators (the transmission scanning approach). Optical scanning performance of the system is determined analytically by use of the extended ray transfer matrix method, leading to two different optical configurations, relying either on a ball lens or plano–convex microlenses. The presented system is aimed to be a core component of miniature MOEMS-based optical devices, which require a 3D optical scanning function, e.g., miniature imaging systems (confocal or optical coherence microscopes) or optical tweezers. © 2015 Optical Society of America

OCIS codes: (230.0230) Optical devices; (220.0220) Optical design and fabrication; (080.0080) Geometric optics; (110.0110) Imaging systems; (130.3990) Micro-optical devices; (180.0180) Microscopy.

http://dx.doi.org/10.1364/AO.54.006924

1. INTRODUCTION

Optical scanning is a common technique employed in optical instrumentation to encode spatial optical signals into temporal ones (optical or electrical) and vice versa. It is used in many different optical sensing systems in which each point of the investigated object is observed or probed (illuminated by light) at different times. Important systems employing optical scanning are 3D imaging devices, such as confocal microscopes or optical coherence tomography [1,2]. These instruments probe the sample with a focused light beam and collect its optical response point by point. Another application of spatial control of light beams is optical tweezers. In this technique, the focused beam is used for trapping and manipulating microparticles, exploiting the mechanical interaction between light and matter [3].

Classical (macro) optical instruments use different scanning techniques that vary in accessible speed, provided resolution, and complexity of the system. One of the most common scanning techniques relies on moving mirrors that can be displaced in the continuous mode (by the so-called rotating polygons) or actuated in the oscillatory mode employing galvanometric servos. Alternative optical scanning systems use acusto-optic deflectors or a setup of movable microlens arrays. An exhausting review of the different scanning architectures can be found in [4].

Because of the key characteristics of optical scanners, a strong effort has been made to improve (or replace) the existing scanning constructions in terms of size, accessible speed, provided resolution, etc. Therefore, optical scanners have become one of the main applications in micro-opto-electro-mechanical systems (MOEMS) technology. This is due to the high potential of MOEMS for the fabrication of scanning micromechanisms, especially based on micromirrors, with inherently low inertia and hence high-speed movement capabilities. Moreover, wafer-level processing allows for the parallel fabrication of MOEMS micro-optical scanners with high yield and throughput, leading to a significant decrease in cost.

The achievements of MOEMS technology can be used to fabricate cheap and miniature devices, working in classical

 © 2015 Optical Society of America

optical instruments as independent scanning modules [5]. However, MOEMS' potential can be exploited much further in the construction of a new type of complete, highly miniaturized optical instrument.

The considered devices are miniature confocal microscopes [6] or OCT imaging systems [7]. These have a large potential for applications for *in vivo* biomedical investigations in microendoscopy [7–9] or miniature handheld devices [10,11]. Highly miniaturized optical instruments can also be used in combination with microfluidic systems to add integrated optical functionality to lab-on-chip devices, such as 3D cell imaging [12] or particle trapping and manipulating [13]. The miniaturization of such systems includes not only scaling down the sizes of the components but also the minimization of the number of elements and the simplification of their arrangement. Moreover, adaptation of the optical system to fabrication technology is crucial.

In this work we focus on a system that allows, as much as possible, the use of the advantages of the parallel (wafer-level) fabrication principle. This is a step forward with respect to most of the miniaturized optical devices in existence today, where different parts of the system are fabricated using different technologies. Indeed, several different highly miniature optical scanning systems were proposed in the literature, but most of them are based only partially on wafer-level technologies and require assembly and packaging procedures realized during different fabrication processes [14–17]. The main advantages of this approach for the device construction are the high level of miniaturization, array ability, and batch fabrication that can result in low-cost devices in the case of high volume production. The main constraint on the vertical architecture of the system is the transmissive scanning that requires an adequate design of the optical train.

2. DESIGN SPECIFICATION FOR A WAFER-LEVEL FABRICATED SYSTEM

The most common beam scanning method employed in miniature systems is based on beam deflection using mirror scanners [6,14–16]. However, this standard technique cannot be easily adapted to the vertical architecture of the complete optical microsystem. Consequently, the discussed system is based on an alternative scanning method in which the transversal and axial movements of the microlenses result in lateral and axial displacements of a focused beam. Several constraints have to be taken into account to implement this method.

The first constraint is the scale of the considered micro-electro-mechanical components that specifies the dimensions of the employed optical elements as well as the possible distances between them. From the point of view of the optical design, the possible sizes and accessible space for the positions of the optical elements are crucial. For instance, the typical thickness of silicon substrates ranges from 0.3 to 1.5 mm. As a consequence, the thicknesses of the employed lenses cannot exceed a few hundred microns, and in vertical architecture, they have to be arranged with small separation distances corresponding to accessible wafer thicknesses.

The considered system employs in-house-made silicon actuators as the active parts of the scanning system (Fig. 1).

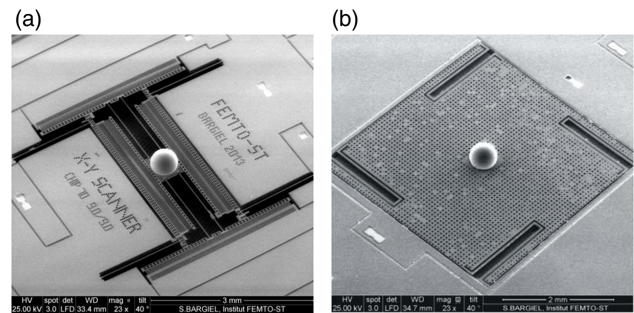

Fig. 1. Micro-electro-mechanical systems microactuators for a 3D optical microlens scanner. (a) The comb-drive-based actuator realizing in-plane (XY) displacement, and (b) the parallel-plate-based actuator for out-of-plane (Z) displacement. Both microactuators have a 500 μm diameter ball microlens on their movable platforms.

The main constraints originating from mechanical scanning, based on these electrostatic actuators, are their limited displacement ranges.

Currently, the displacement amplitudes can reach 35 and 20 μm for in-plane [18] and out-of-plane [19] movements, respectively. Moreover, the micromechanical components are limited in size since the payload to be displaced has to remain as small as possible. This is because the motion speed (scanning frequency) of the system is highly dependent on the mass of the elements placed on the microactuator.

Another important constraint, resulting from the wafer-based fabrication principle, is the alignment accuracy. On one hand, lateral alignment is achieved at the wafer scale by the precise (in the order of microns) pattern transfer by photolithography and wafer-to-wafer bonding [20]. On the other hand, the axial positioning (along the optical axis) of the system components depends on the substrates (wafers) thicknesses. The latter are more difficult to adjust and control, since, for example, wafer-to-wafer thickness dispersion can reach 20 μm and the standard wafer's total thickness variation is 5–10 μm. Thus, it is important to release the tolerances on the axial positioning of the optical elements wherever it is possible.

In addition to the vertical architecture that is defined by the system fabrication philosophy, the main parameters of the optical scanner that are subject to optimization are the scanning volume (3D field of view), resolution (also in 3D space), and working distance (WD).

3. BEAM SCANNING BY LENS DISPLACEMENT

Beam steering, investigated in this work, relies on the movement of lenses as the only means to displace the focused spot inside the scanning volume. This approach was chosen because of its natural straight (linear) geometry, which is well suited for wafer-level fabrication workflow as demonstrated by Kwon and Lee [21].

A focused beam, generated by a single lens, can be axially displaced by the movement of the lens along its optical axis [Fig. 2(a)], while lateral movement of the beam focus can be obtained by the lateral displacement of the lens [Fig. 2(b)]. Paraxial optics can be used [22] for the description of the

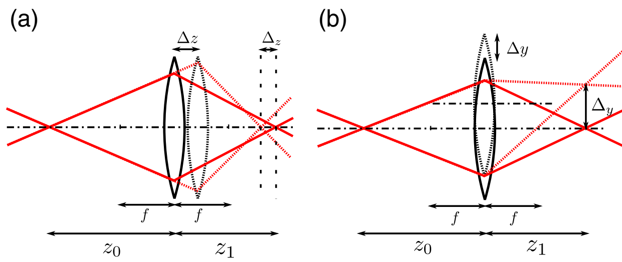

Fig. 2. Focus scanning by single lens displacement. A single lens is used for beam focus displacement in the case of (a) axial and (b) lateral lens displacements.

scanning behavior of a single lens setup. The axial scanning relation is defined by the thin lens equation

$$\frac{1}{f} = \frac{1}{z_0} + \frac{1}{z_1}, \tag{1}$$

where f is lens focal length, and z_0 and z_1 are the distances (relative to the lens) of the beam focus before and after the lens, respectively (Fig. 2). Lateral scanning is described by the geometric formula

$$\frac{\Delta y}{z_0} = \frac{\Delta_y - \Delta y}{z_1}, \tag{2}$$

where Δy is the lens displacement relative to the beam propagation axis, and Δ_y is the resulting lateral displacement of the focus.

The displacement of the beam focus highly depends on the optical configuration, i.e., the position of the lens in regards to the impinging beam convergence point (distance z_0). Scanning relations, defined as magnifications of focus displacements (Δ_y, Δ_z) relative to the lens displacements $(\Delta y, \Delta z)$, are plotted in Fig. 3. We can see that depending on z_0, the scanning magnification changes significantly. In the case of a collimated input beam ($|z_0| \gg f$), magnifications approach unity, whereas in the vicinity of $z_0 = f$, magnifications are very high. In addition to the magnification, an important parameter is the absolute position of the generated focus (z_1). In the same plot (Fig. 3), we can see that z_1 has same convergence points as scanning magnifications, i.e., for $|z_0| \gg f$, $z_1 \to f$, and for $z_0 \to f$, $z_1 \to \infty$

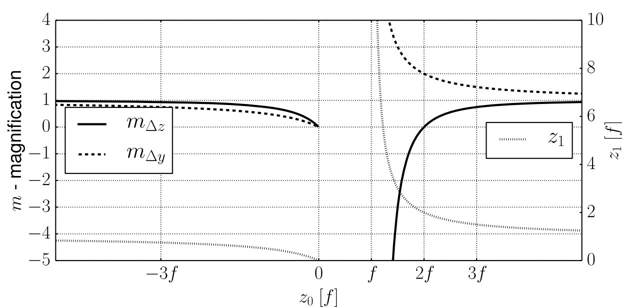

Fig. 3. Lens scanning characteristics. Magnification of the lens axial displacement ($m_{\Delta z} = \frac{\partial \Delta_z}{\partial \Delta z}|_{\Delta z \to 0}$, solid curve) and magnification of the lens lateral displacement ($m_{\Delta y} = \frac{\Delta_y}{\Delta y}$, dashed curve) both functions of the beam divergence (convergence) position relative to the lens (z_0), plotted together with the resulting focus position (the dotted curve with the scale on the right).

(collimated output beam). As a consequence, magnifications can be achieved for $z_0 \in (f, \frac{3}{2}f]$. However, under these conditions, the focused beam is then located relatively far from the lens. This leads to a low numerical aperture for the setup, which in turn leads to a low resolution (large spot size) of the optical system. These simple considerations set the first stage of the system optical design which will look for the best trade-off between magnification (i.e., scanning range) and resolution.

4. 3D BEAM SCANNING BY LENS MOVEMENT

Our system targets to perform beam scanning in three dimensions. For this purpose, the simplest solution would be to perform 3D movement of a single microlens. However, the realization of 3D motion of micro-optical elements is not an easy task. Only very limited types of microactuators are able to provide simultaneous 3D Cartesian movements [23]. An alternative possibility is to use the displacement of two or more lenses to obtain multidimensional optical scanning [21,24].

A. Afocal Doublet for 3D Beam Scanning

In this work, we consider only one of the many possibilities of the implementation of 3D scanning by multilens displacement. The base of the considered system is two separate movements of microlenses: an "in-plane" displacement (the XY plane perpendicular to the optical axis of the lens), and an "out-of-plane" displacement (along the z axis, parallel to the optical axis of the lens).

Consequently, the 3D scanner is based on two movable micolenses. Hence, many different configurations exist for the coupling of the two microlens/movements to obtain 3D scanning. Our choice was oriented by technological constraints and is based on a two-lens afocal setup. In such a system, a collimated beam enters the scanner and axial or lateral lens movements result in decollimation or tilting of the output beam.

The schemes of two possible setups of the scanner working in the afocal configuration are presented in Fig. 4. The two systems differ in terms of the actuators' order. The first setup [Fig. 4(a)], the so-called Z-XY configuration, is made with the axial actuator (Z-scanner), located before the in-plane actuator. In the second system (XY-Z configuration), the actuators' order is inverted [Fig. 4(b)].

The important advantage of an afocal system is that the use of incident/output nearly collimated beams releases axial positioning tolerances between the scanner and preceding/succeeding elements of the system. This is especially important in the wafer-based fabrication, in which axial positioning is usually adjusted by the wafer thicknesses of the building blocks.

This afocal doublet itself does not provide focusing power if the incident beam is collimated. Thus, an additional fixed focusing element is needed to obtain practical 3D beam scanning: the focusing block (the objective). Finally, a collimation block is also required if a point-like light source is considered.

B. Four Lens Setup for Scanning and Focusing

Consequently, in the following we consider the 3D scanning system composed of three functional blocks: a collimation block, used to collimate the light from a point-like source; a scanning block, composed of the actuated lenses arranged in the afocal configuration and responsible for the beam steering;

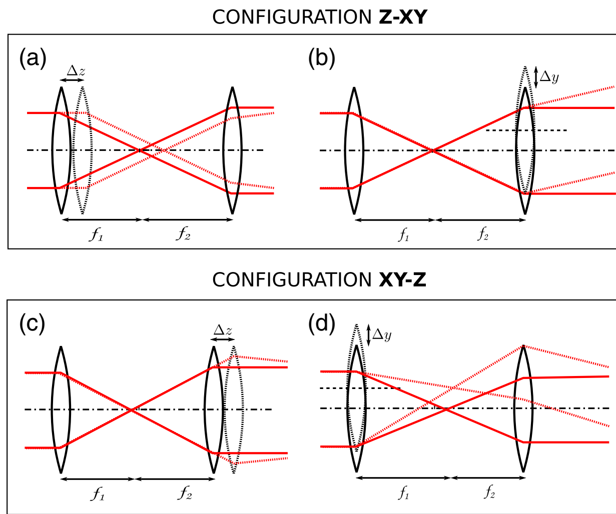

Fig. 4. Afocal systems for 3D beam scanning. Two lenses, separated by a distance equal to the sum of their focal lengths, are used as a scanning system. The displacement of a lens along the optical axis in (a) and (c) adds curvature to the output beam, whereas the lens lateral displacement in (b) and (d) produces a tilt in the output collimated beam. The two configurations are possible with different lens movement orders.

and finally a focusing block, responsible for the generation of the focused spot at the output of the system. The schematic design of the system is presented in Fig. 5.

Figure 5 reveals the advantages of using an afocal system for the scanning function. The active part of the system based on microactuators is located in the center of the system and can be easily protected from the environment. The light path is relatively simple, and since collimated beams are employed, tolerances on the axial distances are loosened. Moreover, if a 3D scanner is used, e.g., for confocal microscopy, additional optical elements, such as a beam splitter [25] or dichroic filter, can be easily added when placed in the collimated beam.

The scanner is thus based on two microlenses that are assembled onto microactuators that can be independently moved from each other. The fragile micromechanical systems can be sealed in a hermetic package, made of the other optical elements (lenses L0 and L3), located at each end. The separation of scanning and focusing functions into two separate parts allows for a more flexible design and fabrication of the device.

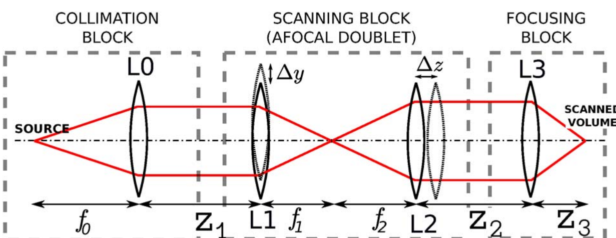

Fig. 5. Layout of the four-lens scanning system. Collimation and focusing lenses added to an afocal scanning doublet for 3D beam scanning. The two lenses located in the center of the system (i.e., L1 and L2) are movable so that L1 can be displaced in-plane (XY) and L2 can be moved along the optical axis.

In particular, since most of the optical parameters of the device can be defined by the proper choice of the focusing lens, the scanning block can be left unchanged for different applications that require different resolutions or scanning ranges.

C. Paraxial Description of the Lens Scanning System

The optical scanning behavior of the proposed system can be analyzed with the ABCD-EF matrix formalism [26]. The method is a classical ABCD ray transfer matrix method, extended to handle shift–tilt transformations of the optical components in the optical train. The standard ABCD ray transfer matrix handles only centered axially symmetric systems, i.e., it transforms the paraxial ray described by its height at the pupil h_{in} and incident angle α_{in}, according to the optical system parameters. These parameters are described by the coefficients in the transformation matrix $\mathbf{M}$:A, B, C, D. In the case of optical setups, consisting of decentered or tilted elements, extended matrix formalism has to be used. Equation (3) describes the ray transformation in such a system, where the additional matrix elements E and F are used to describe the shift and tilt, respectively, present in the nonaxial optical system:

$$\begin{bmatrix} h_{\text{out}} \\ \alpha_{\text{out}} \\ 1 \end{bmatrix} = \underbrace{\begin{bmatrix} A & B & E \\ C & D & F \\ 0 & 0 & 1 \end{bmatrix}}_{\mathbf{M}} \cdot \begin{bmatrix} h_{\text{in}} \\ \alpha_{\text{in}} \\ 1 \end{bmatrix}. \quad (3)$$

The matrix representing the considered system $\mathbf{M_{sys}}$ is constructed from matrices, which describe each element composing the system. As mentioned before, the system can be divided into three parts: collimation block, scanning block, and focusing block. Then, $\mathbf{M}_{\text{sys}} = \mathbf{M}_{\text{foc}} \cdot \mathbf{M}_{\text{scan}} \cdot \mathbf{M}_{\text{col}}$. Similarly, the matrix representing the scanning block, i.e., M_{scan}, can be expressed as a multiplication of matrices representing components of the block. Two scanner configurations are possible (Fig. 4) and result in different ray transformation matrices expressed by Eq. (4) for the "XY-Z" configuration and Eq. (5) for inverted scanner configuration ("Z-XY"):

$$\mathbf{M}_{\text{scan}}^{(xy\text{–}z)} = \underbrace{\mathbf{M}_{\Delta z}\mathbf{M}_{L2} \cdot \mathbf{M}_{-\Delta z}}_{\text{axially displaced } L2} \cdot \mathbf{M}_{z_2} \cdot \underbrace{\mathbf{M}_{\Delta y} \cdot \mathbf{M}_{L1} \cdot \mathbf{M}_{-\Delta y}}_{\text{laterally displaced } L1}, \quad (4)$$

$$\mathbf{M}_{\text{scan}}^{(z\text{–}xy)} = \underbrace{\mathbf{M}_{\Delta y}\mathbf{M}_{L2} \cdot \mathbf{M}_{-\Delta y}}_{\text{laterally displaced } L2} \cdot \mathbf{M}_{z_2} \cdot \underbrace{\mathbf{M}_{\Delta z} \cdot \mathbf{M}_{L1} \cdot \mathbf{M}_{-\Delta z}}_{\text{axially displaced } L1}. \quad (5)$$

For sake of simplicity and to investigate the general behavior of the proposed optical system, all lenses are modeled with the thin lens approximation $\mathbf{M_{lens}} = \begin{bmatrix} 1 & 0 & 0 \\ -f^{-1} & 1 & 0 \\ 0 & 0 & 1 \end{bmatrix}$, where f is the lens focal length. The free space propagation is described by $\mathbf{M_{\Delta z}} = \begin{bmatrix} 1 & \Delta z & 0 \\ 0 & 1 & 0 \\ 0 & 0 & 1 \end{bmatrix}$, where z_i is the propagation distance.

The coordinate shift is $\mathbf{M_{\Delta y}} = \begin{bmatrix} 1 & 0 & \Delta y \\ 0 & 1 & 0 \\ 0 & 0 & 1 \end{bmatrix}$, where Δy defines the element's shift perpendicular to the propagation axis. Consequently,

$$\mathbf{M}_{\text{scan}}^{(xy\text{-}z)} = \begin{bmatrix} \frac{(-\Delta z^2+\Delta z f_2-f_2^2)}{f_1 f_2} & \frac{\Delta z^2-\Delta z f_1+(f_1+f_2-\Delta z)f_2}{f_2} & \frac{(\Delta z^2-\Delta z f_1-\Delta z f_2+f_1 f_2+f_2^2)}{f_1 f_2}\Delta y \\ -\frac{\Delta z}{f_1 f_2} & \frac{(\Delta z-f_1)}{f_2} & \Delta y \frac{(\Delta z-f_1)}{f_1 f_2} \\ 0 & 0 & 1 \end{bmatrix}, \tag{6}$$

$$\mathbf{M}_{\text{scan}}^{(z\text{-}xy)} = \begin{bmatrix} -\frac{(\Delta z+f_2)}{f_1} & \frac{\Delta z(\Delta z+f_2)+f_1(\Delta z+f_1+f_2)}{f_1} & 0 \\ \frac{\Delta z}{f_1 f_2} & \frac{(-\Delta z^2+f_1 f_2-f_1(\Delta z+f_1+f_2))}{f_1 f_2} & \frac{\Delta y}{f_2} \\ 0 & 0 & 1 \end{bmatrix}. \tag{7}$$

From Eqs. (6) and (7), we can extract the most important scanner properties. First, the axial displacement of lens L2 leads to decollimation of the scanning block output beam. The focal length of the scanner f_{scanner} is proportional to the inverse of axial lens displacement:

$$f_{\text{scanner}} = \frac{f_1 f_2}{\Delta z}. \tag{8}$$

Second, the lateral displacement of the lens L1 provokes the tilting of the output beam such as

$$\delta_y^{xy-z} = \Delta y \frac{\Delta z - f_1}{f_1 f_2}, \tag{9}$$

$$\delta_y^{z-xy} = \frac{\Delta y}{f_2}. \tag{10}$$

D. Scanning Performance

The scanning performance is defined as the scanning range in all three dimensions, which depends only on the scanning doublet and the objective lens (L3). From the total system matrix M_{sys}, we can get the "scanning equations," i.e., equations that define the displacement of the focal spot as a function of the lenses' displacements Δy, Δz and the system configuration f_i and z_i. The scanning performances are

$$\Delta_z^{(xy-z)} = \Delta z \frac{f_3^2}{\Delta z^2 + f_2^2 + \Delta z(z_3 - f_2 - f_3)}, \tag{11}$$

$$\Delta_y^{(xy-z)} = -\Delta y \frac{f_2 f_3}{\Delta z^2 + f_2^2 + \Delta z(z_3 - f_2 - f_3)}. \tag{12}$$

The scanning volume is then located in the vicinity of the focus point of the objective lens (L3). Thus, the focus position is defined by the $L3$ focal length and the displacement is due to the scanner, so that $z_{\text{foc}} = f_3 + \Delta_z$. In the case of the inverse scanner configuration ("Z-XY"), scanning relations are slightly different:

$$\Delta_z^{z-xy} = -\Delta z \frac{f_3^2}{\Delta z(z_3 - f_2 - f_3) - f_2^2}, \tag{13}$$

$$\Delta_y^{z-xy} = \Delta y \frac{f_3(\Delta z + f_2)}{\Delta z(f_2 + f_3 - z_3) + f_2^2}. \tag{14}$$

An important characteristic of the scanner is the nonlinearity of the axial scanning [Eqs. (11) and (14)]. As presented in Fig. 6(a), axial scanning is slightly nonlinear where nonlinearity depends on system parameters [Eq. (11)]. Lateral scanning, according to Eq. (12), is linear in Δy. However, it is also coupled to axial scanning [Fig. 6(b)]. This effect defines the shape of the scanning volume. In the ideal case, i.e., linear and not coupled, scanning would generate a scanning volume in the form of a cuboid. But, the nonlinearity and coupling effect lead to a scanned volume having a more complex shape [Fig. 7(a)]. Then, it can be noted that it is preferable to set $z_3 = f_2 + f_3$ in order to minimize these effects [Figs. 6(b) and 7], although complete linearization can be achieved only with the "Z-XY" configuration. Nevertheless, the scanning coupling and nonlinearity are of the second order. Then, simpler linear scanning relations can be written in the approximation of the small lenses' displacements, Eqs. (15) and (16), that hold for both configurations of the scanner system:

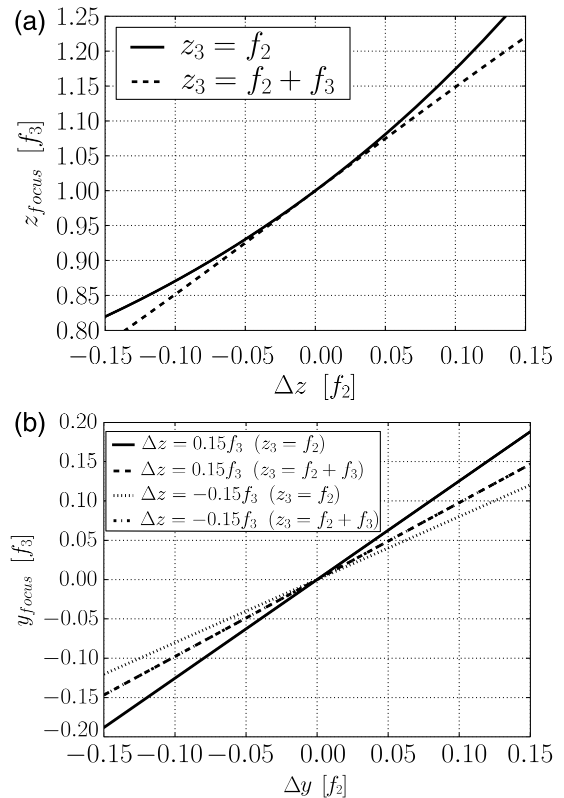

Fig. 6. Afocal scanner paraxial scanning behavior. (a) The nonlinear dependence of scanning in the axial direction and (b) the coupling effect in the case of simultaneous axial and lateral scanning. In the Z-XY setup, nonlinearity can be canceled [dashed line in (a)] and coupling minimized when z_3 is chosen as ($z_3 = f_2 + f_3$) [dashed and dashed–dotted lines overlapping in (b)]. Plots for the system with $f_3 = \frac{3}{2} f_2$.

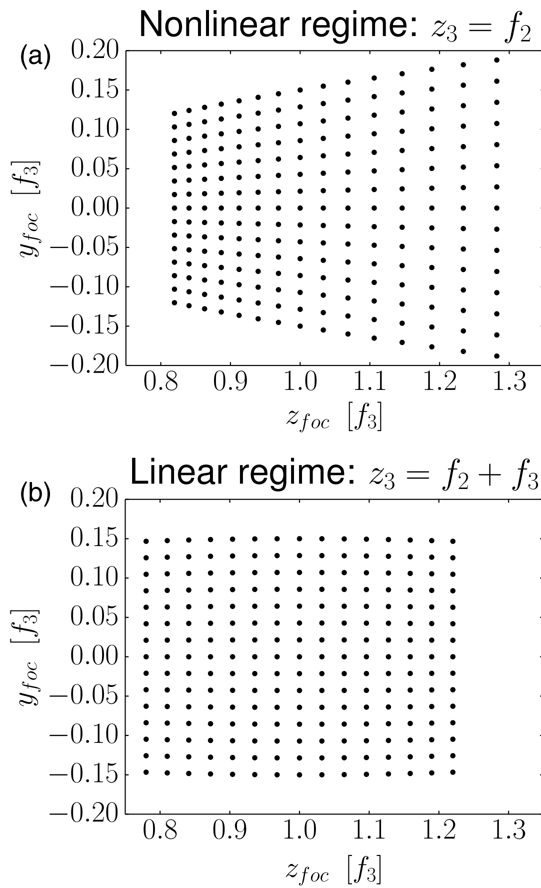

Fig. 7. Paraxial prediction of the shape of scanning volume. Scanning zones (yz cross section) for the two cases: (a) $z_3 = f_2$, resulting in a visible coupling and nonlinearity of the scanning; and (b) with $z_3 = f_1 + f_2$, where coupling is suppressed and nonlinearity is minimized. Each drawn point corresponds to the unit displacements of the scanning lenses in y and z directions.

$$\Delta_z \approx \Delta z \left(\frac{f_3}{f_2}\right)^2, \tag{15}$$

$$\Delta_y \approx \Delta y \frac{f_3}{f_2}. \tag{16}$$

It is visible that the scanning performance depends mostly on the ratio $\frac{f_3}{f_2}$ for both considered cases. Consequently, in order to amplify the scanning amplitude, f_3 should be chosen higher than f_2. However, resolution is defined by the system's NA [Eq. (17)] which is proportional to $\frac{f_2}{f_3}$ that is an inverse of the dependence of the scanning performance

$$\text{NA} \approx \frac{h_3}{f_3} = \frac{h_1}{f_1}\left(\frac{f_2}{f_3}\right). \tag{17}$$

This implies that it is not possible to maximize both scanning volume and resolution at the same time using only f_2/f_3 as a parameter [27].

The derived paraxial formulas aimed at analyzing the scanning performance of the two possible configurations have been considered. From the optical point of view, their scanning properties are very similar. However, an important difference appears when the scanning doublet is considered along with the focusing block. In the Z-XY configuration, the position of the beam center leaving the scanner follows the position of the XY scanning lens, whereas in the case of XY-Z configuration, the beam center only slightly changes in the focal plane of $L2$ where only a tilt of the optical axis is generated (Fig. 4). This allows for a more flexible, and optically optimal, use of the focusing block in the complete system. Moreover, from the perspective of microfabrication, system construction and integration depends strongly on the scanners' order. In the considered system, microactuators are enclosed between collimation and focusing blocks, then the electrical connections required for the actuators' control have to be implemented through the wafers of both micromechanical systems. Since the XY-scanner is more complex and requires more electrical connections than the Z-scanner, the XY-Z order allows for the minimization of the number of electrical through wafer connections. As was discussed before, one advantage of the Z-XY configuration is the possibility of linearization of the scanning zone; that is not entirely possible within the XY-Z setup. However, although the complex shape of the scanning zone is inconvenient, it can be acceptable provided that appropriate data postprocessing is employed to remap the actuators' positions to the scanned volume. As a consequence, the following optical implementations are focused on the XY-Z configuration only.

5. NONPARAXIAL ANALYSIS AND SCANNER IMPLEMENTATIONS

While the paraxial analysis allowed for the description of the scanning behavior and the evaluation of the scanning performances of the system as a function of the lenses' parameters, the complete system performance is defined by the amount of optical aberrations present in the system. Thus, a high NA with a minimum of aberrations is required to reach high resolution. In general, the on-axis aberrations (mainly spherical aberration) limit the accessible system resolution, and off-axial aberrations (mainly astigmatism and coma) limit the lateral scanning range of the system. In the following, the aberration analysis and design optimization is performed with ZEMAX software.

A. Scanner Based on Ball Lenses

The first investigated implementation of our system is based on discrete micro-optical components that are assembled onto the microactuators by means of the pick-and-place principle. This hybrid approach (wafer-level fabrication of actuators and the use of discrete microlenses) largely simplifies the fabrication technology since actuators can be fabricated with standard silicon-based micromachining. However, the available elements that can be used in the considered system only exist in limited geometrical forms. The most common microlenses commercially available are the so-called ball lenses. These types of elements are mostly used in fiber optics systems to couple light into fibers or for fiber-to-fiber interconnections [28]. Because of their well-defined geometry and their good optical quality, they were already employed in optical micro-electromechanical systems (MEMS) in embedded fiber switches

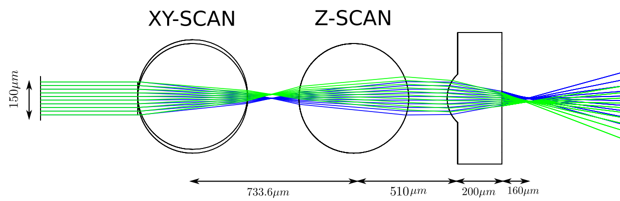

Fig. 8. Ray tracing through a ball-lens-based scanner. The scanner is composed of two identical ball lenses $f_{BL} = 366.8$ μm and a focusing lens (ROC = 150 μm, diameter 220 μm). Ray tracing is shown for two cases: no lens-displacement (blue rays) and a 17.5 μm displaced XY scanning lens (green rays).

[29,30] or as simple high NA objectives [31]. Another important advantage of ball lenses is their ability to self-align, which is important in the case of the pick-and-place assembly process. For these reasons, the first considered system employs commercially available ball microlenses as scanning lenses.

The optical design of the scanner is presented in Fig. 8. Two movable ball lenses (500 μm in diameter, made from N-BK7 glass, from Edmunds) compose the discussed scanning doublet, with the setup in the XY-Z configuration. The collimated input beam (150 μm diameter) impinges the first lens, which is placed on a laterally movable stage. The second lens that can be displaced along the system optical axis recollimates the beam, which is finally focused by the last lens. The spherical plano–convex focusing lens is made within the wafer-level approach using the silicon/glass molding technique [32].

The presented system (Fig. 8) is characterized by a working distance WD ≈ 160 μm and a numerical aperture NA = 0.25 that would provide, in the diffraction-limited case, a focal spot of the order of $\delta_{x_{\mathrm{airy}}} = 1.5$ μm. However, aberrations present in the system are responsible for the degradation of optical performance. The used components and limited positioning freedom do not allow much liberty for system optimization.

All optical elements in the system contribute to the spherical aberration, although the main contribution is brought by the focusing lens. However, the main limitation of the system performance appears when lateral scanning is considered. In Fig. 9, the contrast transfer function is presented for the system in three cases: the axial case (all lenses aligned on-axis) and two lateral scanning positions ($\Delta y = 17.5$ μm and $\Delta y = 35$ μm).

Table 1. System Performance Statistics for the Ball Lens Scanner[a]

Δy [μm]	0	17.5	35
$\sigma_{\mathrm{RMS}}[\lambda]$	0.06	0.09	0.18
$Z_6[\lambda]$	—	−0.035	−0.13
$Z_7[\lambda]$	—	−0.069	−0.11
$Z_{11}[\lambda]$	0.06	0.05	0.033
SR	0.87	0.71	0.27
δ_x [μm]	1.9	1.9	3.7
δ_y [μm]	1.9	2.2	3.8

[a]Aberration analysis made within the Zernike wavefront expansion quantifies the effect of lateral scanning (Δy dependence) on optical performance of the system. The principal Zernike terms that contribute to the total wavefront error (σ_{RMS}) are considered, i.e., Z_6, astigmatism; Z_7, coma; and Z_{11}, spherical aberration (in all calculations $\lambda = 670$ nm). The Strehl ratio (SR) is also indicated. The resolutions $\delta_{x/y}$ are derived from the system MTF with a 0.2 contrast criteria.

Resolution in the on-axis case is reasonably close to the aberration-free system (i.e., diffraction limited). However, lateral scanning visibly deteriorates the system performance. In particular, for large lateral lens displacements, off-axial aberrations (coma, astigmatism) deform the focal spot, resulting in a different resolving power along the two perpendicular directions. This resolution is always worse along the scanning direction.

The effects of aberrations on the system resolution (lateral spot size) is visible in the so-called "spot diagram." The spot diagram for the discussed system is presented in Fig. 10. Off-axis aberrations are visible when lateral scanning is considered, leading to enlarged and deformed focus spots [Figs. 10(b) and 10(c)]. The wavefront analysis for the three considered cases (Table 1) also shows that wavefront error σ_{rms} changes drastically with a lateral scan and that astigmatism and coma are the main aberration terms involved.

As was discussed before, displacement of the lenses in the scanning doublet is, in general, nonlinear and coupled. In addition, the scanning surface tends to be curved due to optical aberrations. The exact shape of the scanned volume is important since it allows one to relate the positions of the lenses (defined by the scanners positions) to the location of the focused spot generated by the system. The X–Z cross section of the scanned volume is schematically presented in Fig. 11. The resulting shape originates from the combination of paraxial

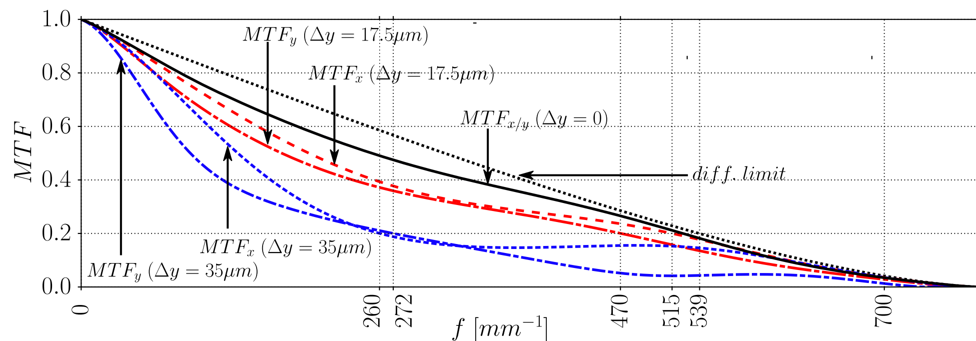

Fig. 9. Ball-lens-based scanner. Modulation transfer function plotted for three scanner states: coaxial state ($\Delta y = 0$) (black solid curve), states with scanning lens (L1) displaced by $\Delta y = 17.5$ μm (red curves) and $\Delta y = 35$ μm (blue curves). For comparison with the ideal system, diffraction limit is also indicated (black dotted curve). MTF_y and MTF_x represent the MTF cross sections along and perpendicular to the direction of the lens displacement, respectively.

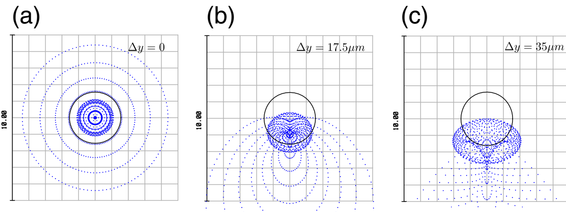

Fig. 10. Spot diagrams of the ball lens scanning system. The impact of the aberrations on the geometrical (ray-traced) focus spot in the case of (a) $\Delta y = 0$, (b) $\Delta y = 17.5$ μm, and (c) $\Delta y = 35$ μm of the lateral displacement of the first scanning lens. The circle drawn in each spot diagram represents the Airy disk of the radius defined by the NA of the system (1.5 μm).

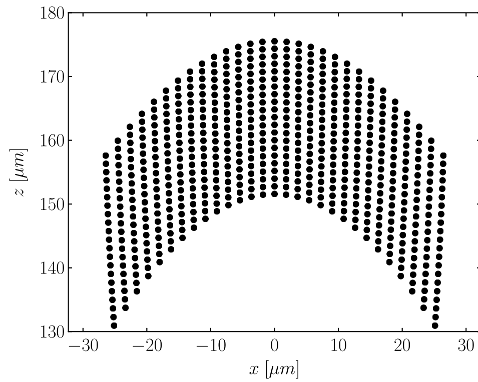

Fig. 11. Shape of the scanning volume of the ball-lens-based system. The curved scanning volume resulting from off-axis aberrations present in the system calculated by ray tracing within ZEMAX. Adjacent points correspond to the scanning lenses displaced by 2 μm for two considered (x, z) directions.

scanning coupling, classical image curvature (Petzval curvature), and on a specific dependence of astigmatism on lateral scanning.

B. Scanner Based on Plano–Convex Aspherical Lenses

Ball lenses as a part of the scanning doublet are not an optimal solution. First, aberrations generated by the scanner, in particular, astigmatism and coma appearing during lateral scanning, seriously deteriorate the resolution of the system in the edges of the scanning zones. Second, ball lenses cannot be integrated onto the MEMS scanner with batch-fabrication processes, and the inconvenient pick-and-place scheme has to be employed for the system construction.

For these reasons, a more optimal design, investigated in this work, is based on plano–convex lenses. However, similar to ball lenses, plano–convex lenses having spherical shapes always lead to poor off-axis performances. One solution to improve scanner optical performance is to use aspherical lenses.

Figure 12 displays the scanning system where ball lenses have been replaced by two aspheric, conic microlenses, whose geometry is optimized to minimize system aberrations. As previously, the focusing objective remains a spherical microlens.

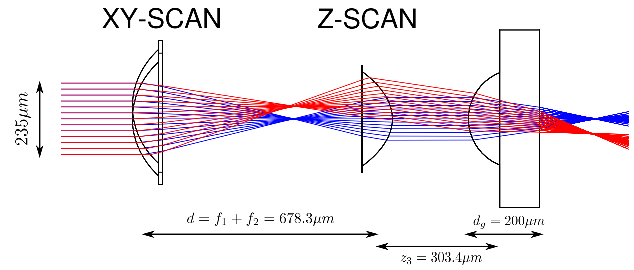

Fig. 12. Ray tracing through the plano–convex lens-based scanner. The scanner is composed of two plano–convex aspherical lenses, placed in the afocal configuration. The blue rays correspond to an aligned system, whereas the red rays correspond to a system in which the first lens is laterally displaced by 35 μm.

The afocal scanning doublet was optimized as a separate block. Its magnification was chosen to be less than 1.0 to allow the use of a larger input beam than in the case of the ball lens setup (limited to 150 μm). Based on ZEMAX optimization, the best conic constants of the doublet were found to be $k_1 = -0.314$ and $k_2 = -0.859$ for lenses fixed in the afocal configuration. Their radii of curvature should then be $R_1 = 200$ μm and $R_2 = 110$ μm, their thickness $d_l = 85$ μm, and their diameters $D_1 = 370$ μm and $D_2 = 275$ μm. The considered lenses are expected to be made of Borofloat33 (Schott, Germany) glass.

Although microlenses with negative conic constant have been already fabricated within different microfabrication technologies [33–37], precise control of their shape is challenging and the possibility of aspherizing the geometry of usual spherical microlenses highly depends on the employed fabrication technology.

The tolerances concerning these conic constants for lenses of the afocal doublet are presented in Fig. 13, where the wavefront error is plotted as a function of the conic constants of the two microlenses. It can be noted that the wavefront deviation should remain lower than 0.05λ in order to obtain diffraction-limited performance within the scanning doublet. Moreover,

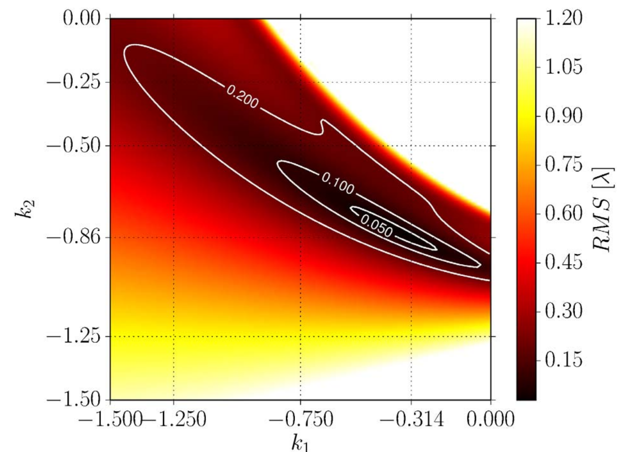

Fig. 13. Aspherical scanning doublet: conic constant's tolerances. The impact of the conic constant on the optical performance (via σ_{RMS}) of the scanning block.

Table 2. Plano–Convex-Lenses-Based Scanning System Performance Summary[a]

Δy [μm]	0	17.5	35
$\sigma_{RMS}[\lambda]$	0.046	0.053	0.070
$Z_6[\lambda]$	—	−0.005	−0.012
$Z_7[\lambda]$	—	−0.002	−0.010
$Z_{11}[\lambda]$	0.05	0.05	0.05
SR	0.92	0.89	0.85
δ_x	2.34	2.38	2.53
δ_y	2.34	2.45	2.94

[a]Same description as in Table 1.

tolerances are wider on the XY scanning lens than on the second z scanning one.

The obtained resolution with such a scanning system and a focusing block based on a spherical microlens ($R_3 = 140$ μm, $d_{glass} = 200$ μm, and $D_3 = 260$ μm) is presented in Fig. 14 by use of the spot diagrams and in Fig. 15 by means of the modulation transfer function. It is visible that this system is characterized by much better off-axis performance than the one based on ball lenses. Table 2 summarizes the optical performance of the system. It can be seen that coma and astigmatism terms decreased by a factor of ten, when compared to the ball-lens-based system.

Finally, lower aberrations generated by the scanning doublet (because of aspheric lenses) as well as the magnification that can be chosen as lower than one (more freedom in the choice of plano–convex lens geometries) allow one to achieve a higher NA within the scanning block. This higher NA within the scanning block, in turn, allows one to reduce the NA of the focusing block without changing the resolution of the entire system. Consequently, a longer focal length of the focusing block can be used to provide better scanning magnification [Eqs. (15) and (16)]. The scanning zone, obtained with the lenses' scanning range of $\Delta y = \Delta x = \pm 35$ μm and $\Delta z = \pm 20$ μm, would then be 84 μm × 84 μm × 60 μm, with the optical resolution below 3.0 μm in the whole scanning volume. Moreover, it can be noted that the scanning zone is less curved (Fig. 16). This is a direct consequence of the astigmatism elimination.

The optical system was analyzed and optimized for monochromatic light ($\lambda = 670$ nm). Although, in practice, light sources are characterized by a finite spectral width for which chromatic aberrations additionally appear. Hence, we

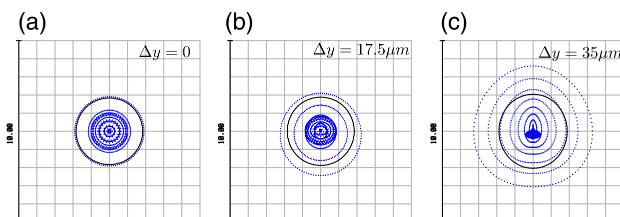

Fig. 14. Plano–convex-lenses-based scanning system: spot diagram. The ray-traced form of the focal spot generated by the scanning system. The circle in the center represents the Airy disk of size $r_{Airy} = 1.99$ μm. The three spots correspond to three lateral positions of the scanner: (a) $\Delta y = 0$, (b) $\Delta y = 17.5$ μm, and (c) $\Delta y = 35$ μm.

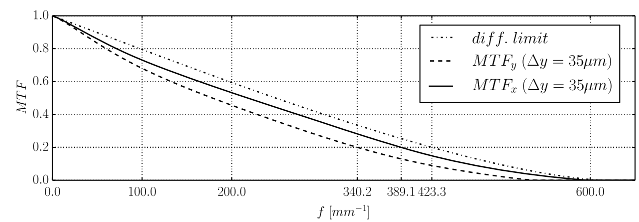

Fig. 15. Plano–convex-lenses-based scanning system. The modulation transfer function for the case of maximal lens displacement. The difference between the diffraction limit (dashed–dotted curve) obtained within this system is significantly lower than in the case of the configuration employing ball lenses (Fig. 9).

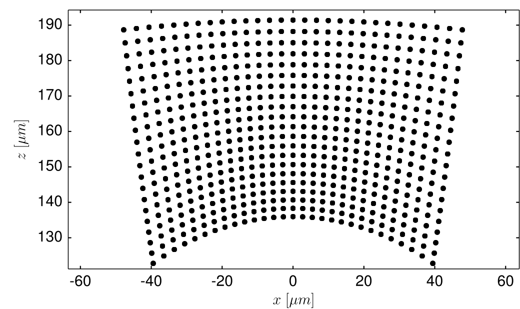

Fig. 16. Plano–convex-lenses-based scanning system: scanned volume shape. XZ cross section of the scanning volume obtained with the aspheric-lenses-based system.

considered a ±0.5 μm deterioration of the system resolution (which is near 2 μm) resulting from the axial chromatic aberration in order to estimate the corresponding acceptable linewidth of the source. In these conditions, the source linewidth is calculated to be ±30 nm and can be considered sufficient for targeted applications such as reflective confocal microscopy or OCT that employs VCSEL or LED as light sources. For larger spectral ranges, it can be noted that chromatic aberrations could probably be compensated by combining lenses with different dispersion parameters or by using hybrid refractive–diffractive optical components.

6. WAFER-LEVEL CONSTRUCTION OF THE SCANNER

The construction scheme of the 3D microlens scanner, based on the first described micro-optical architecture, is presented in Fig. 17. The device is composed of five separately processed wafers that are bonded into a stack. Two silicon wafers are present with micromachined actuators (Fig. 1), and integrated microlenses are located in the center of the system.

The distance between the two scanning lenses is defined by a separation wafer made of low temperature cofired ceramics (LTCC). It allows for reliable bonding with the actuator's substrates and simultaneously provides electrical connections through the bonded stack [38]. The top and bottom lids are made of glass wafers, providing encapsulation of the fragile micromechanical structures. In addition, they support

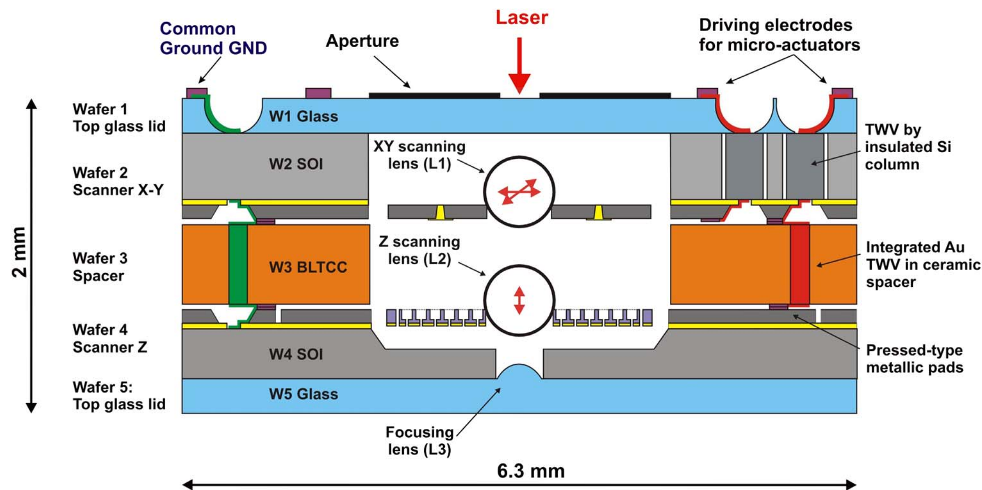

Fig. 17. Scheme of the system construction. Five vertically stacked wafers compose the system. Two silicon wafers (W2 and W4) are the construction substrates for the microactuators. The separation wafer (W3) made of LTCC defines the separation between the scanning lenses (L1 and L2), while glass wafers (W1 and W5) encapsulate the micromechanical components and provide mechanical support for optical components: the aperture stop (W1) and the focusing lens (W5).

optical components, i.e., an aperture stop (W1) and focusing lens (W5).

An important feature of the designed device is that all electrical connections needed to drive electrostatic microactuators, are accessible on the top of the structure [39]. The electrical lines are made vertically as conductive through wafer vias (TWV) or horizontally by employing the low resistivity of silicon. Consequently, the device can be hermetically sealed during the wafer bonding procedure that can significantly improve the reliability and robustness of the micromechanical components [40]. The key fabrication steps concern multiwafer bonding for wafer-level assembly and the electrical interconnection of all components [41,42]. The presented device is fabricated on 4 in. wafers, which leads to the fabrication of 120 devices during a single technological run.

The first presented version of the device employs ball lenses in the scanning block. This choice arises from the simpler fabrication of the actuators and leads to a faster development of multiwafer stacking technologies required for the system. The ball lenses are assembled into the microactuators by pick-and-place and joined to the actuator platform by the laser bonding technique [43].

7. CONCLUSIONS

In this paper, a micro-optical design for a 3D microlens scanner constructed within MOEMS technologies is considered. The technological constraints, related to the employed multiwafer vertical integration approach, were addressed. The proposed system is based on an afocal scanning doublet and uses the displacements of two microlenses to perform 3D optical scanning. Separation of scanning and focusing blocks provides flexibility of the system and releases tolerances for axial positioning of the micro-optical components. Paraxial analysis of the proposed system was performed by use of the extended ray transfer matrix method (ABCD-EF). It provided analytic relations of the 3D scanning system, depending on component parameters and arrangements, and revealed and quantified the coupling of lateral and axial scanning and the inherent nonlinearity of axial scanning.

As a result, two optical configurations were proposed that differ in terms of difficulties of technological realizations as well as in optical performances. The first configuration, based on ball lenses, suffers from off-axis aberrations, which deteriorate the optical resolution on the lateral edges of the scanning volume. However, it allows for the use of commercially available optical components and simplifies the fabrication process of the device. The second configuration relies on plano–convex microlenses with aspherical geometries that allow for the improvement of off-axial behavior of the system.

Microlenses could be fabricated using silicon molding combined with glass reflow technology [32], where advanced silicon etching technology based on reactive ion etching [44,45] could generate molds with aspherical shapes. Such plano–convex lenses could be integrated into the device by means of the wafer-level approach, allowing fabrication of the complete microinstrument by the wafer-level process.

Funding. Agence Nationale de la Recherche; Joint Programme Inter Carnot Fraunhofer PICF; Labex Action.

REFERENCES AND NOTES

1. T. Wilson, *Confocal Microscopy* (Academic, 1990).
2. J. G. Fujimoto, M. E. Brezinski, G. J. Tearney, S. A. Boppart, B. Bouma, M. R. Hee, J. F. Southern, and E. A. Swanson, "Optical biopsy and imaging using optical coherence tomography," Nat. Med. **1**, 970–972 (1995).
3. D. G. Grier, "A revolution in optical manipulation," Nature **424**, 810–816 (2003).
4. L. Beiser, *Unified Optical Scanning Technology* (Wiley, 2005).
5. H. Miyajima, K. Murakami, and M. Katashiro, "MEMS optical scanners for microscopes," IEEE J. Sel. Top. Quantum Electron. **10**, 514–527 (2004).
6. D. L. Dickensheets and G. S. Kino, "Micromachined scanning confocal optical microscope," Opt. Lett. **21**, 764–766 (1996).

7. T. Xie, H. Xie, G. Fedder, and Y. Pan, "Endoscopic optical coherence tomography with new MEMS mirror," Electron. Lett. **39**, 1535 (2003).
8. J. Knittel, L. Schnieder, and G. Buess, "Endoscope-compatible confocal microscope using a gradient index-lens system," Opt. Commun. **188**, 267–273 (2001).
9. C. Liu, C. Q. Li, X. L. Zuo, R. Ji, X. J. Xie, Y. S. Yang, and Y. Q. Li, "Confocal laser endomicroscopy for the diagnosis of colorectal cancer *in vivo*," J. Dig. Dis. **14**, 259–265 (2013).
10. R. Hofmann-Wellenhof, G. Pellacani, J. Malvehy, and H. Soyer, *Reflectance Confocal Microscopy for Skin Diseases* (Springer, 2012).
11. A. A. Tanbakuchi, A. R. Rouse, J. A. Udovich, K. D. Hatch, and A. F. Gmitro, "Clinical confocal microlaparoscope for real-time *in vivo* optical biopsies," J. Biomed. Opt. **14**, 044030 (2009).
12. Z. Göröcs and A. Ozcan, "On-chip biomedical imaging," IEEE Rev. Biomed. Eng. **6**, 29–46 (2013).
13. J. Enger, M. Goksör, K. Ramser, P. Hagberg, and D. Hanstorp, "Optical tweezers applied to a microfluidic system," Lab Chip **4**, 196–200 (2004).
14. K. Kumar, K. Hoshino, and X. Zhang, "Handheld subcellular-resolution single-fiber confocal microscope using high-reflectivity two-axis vertical combdrive silicon microscanner," Biomed. Microdevices **10**, 653–660 (2008).
15. H. Ra, W. Piyawattanametha, M. J. Mandella, P.-L. Hsiung, J. Hardy, T. D. Wang, C. H. Contag, G. S. Kino, and O. Solgaard, "Three-dimensional *in vivo* imaging by a handheld dual-axes confocal microscope," Opt. Express **16**, 7224–7232 (2008).
16. S. Tang, W. Jung, D. McCormick, T. Xie, J. Su, Y.-C. Ahn, B. J. Tromberg, and Z. Chen, "Design and implementation of fiber-based multiphoton endoscopy with microelectromechanical systems scanning," J. Biomed. Opt. **14**, 034005 (2009).
17. Y. Wang, S. Bish, J. W. Tunnell, and X. Zhang, "MEMS scanner based handheld fluorescence hyperspectral imaging system," Sens. Actuators A **188**, 450–455 (2012).
18. K. Laszczyk, S. Bargiel, C. Gorecki, J. Krężel, P. Dziuban, M. Kujawińska, D. Callet, and S. Frank, "A two directional electrostatic comb-drive X–Y micro-stage for MOEMS applications," Sens. Actuators A **163**, 255–265 (2010).
19. S. Bargiel, C. Gorecki, T. Verdot, K. Laszczyk, J. Albero, and L. El Fissi, "Electrostatically driven optical Z-axis scanner with thermally bonded glass microlens," Procedia Eng. **5**, 762–765 (2010).
20. M. Gad-el Hak, *MEMS: Design and Fabrication*, Mechanical and Aerospace Engineering Series (Taylor & Francis, 2010).
21. S. Kwon and L. P. Lee, "Micromachined transmissive scanning confocal microscope," Opt. Lett. **29**, 706–708 (2004).
22. M. Born, E. Wolf, and A. Bhatia, *Principles of Optics: Electromagnetic Theory of Propagation, Interference and Diffraction of Light* (Cambridge University, 1999).
23. L. Wu and H. Xie, "A large vertical displacement electrothermal bimorph microactuator with very small lateral shift," Sens. Actuators A **145–146**, 371–379 (2008).
24. H.-C. Park, C. Song, and K.-H. Jeong, "Micromachined lens microstages for two-dimensional forward optical scanning," Opt. Express **18**, 16133–16138 (2010).
25. M. Baranski, S. Bargiel, N. Passilly, B. Guichardaz, E. Herth, C. Gorecki, C. Jia, J. Frömel, and M. Wiemer, "Wafer-level fabrication of microcube-typed beam-splitters by saw-dicing of glass substrates," IEEE Photon. Technol. Lett. **26**, 100–103 (2014).
26. M. Nazarathy, A. Hardy, and J. Shamir, "Misaligned first-order optics: canonical operator theory," J. Opt. Soc. Am. A **3**, 1360–1369 (1986).
27. We can notice that this is a common rule also in classical microscopy, where improvement in the resolution leads to a decreased field of view.
28. J. Mireles, M. Garcia, and R. Ambrosio, "Packaging investigation and study for optical interfacing of micro components with optical fibers, part I," Superficies Vacio **20**, 21–33 (2008).
29. M. Sasaki, F. Nakai, K. Hane, K. Yokomizo, and K. Hori, "Absolute micro-encoder using image obtained by ball lens assembled inside wafer," J. Opt. A **8**, S391–S397 (2006).
30. C. T. Pan, "Silicon-based coupling platform for optical fiber switching in free space," J. Micromech. Microeng. **14**, 129–137 (2004).
31. Y. J. Fan, Y. C. Wu, Y. Chen, Y. C. Kung, T. H. Wu, K. W. Huang, H. J. Sheen, and P. Y. Chiou, "Three dimensional microfluidics with embedded microball lenses for parallel and high throughput multicolor fluorescence detection," Biomicrofluidics **7**, 044121 (2013).
32. J. Albero, L. Nieradko, C. Gorecki, H. Ottevaere, V. Gomez, H. Thienpont, J. Pietarinen, B. Päivänranta, and N. Passilly, "Fabrication of spherical microlenses by a combination of isotropic wet etching of silicon and molding techniques," Opt. Express **17**, 6283–6292 (2009).
33. W. Däschner, "General aspheric refractive micro-optics fabricated by optical lithography using a high energy beam sensitive glass gray-level mask," J. Vac. Sci. Technol. B **14**, 3730–3733 (1996).
34. D. W. de Lima Monteiro, O. Akhzar-Mehr, P. M. Sarro, and G. Vdovin, "Single-mask microfabrication of aspherical optics using KOH anisotropic etching of Si," Opt. Express **11**, 2244–2252 (2003).
35. D. Wu, Q. Chen, L. Niu, J. Jiao, H. Xia, J. Song, and H. Sun, "100% fill-factor aspheric microlens arrays (AMLA) with sub-20-nm precision," IEEE Photon. Technol. Lett. **21**, 1535–1537 (2009).
36. R. Voelkel, "Wafer-scale micro-optics fabrication," Adv. Opt. Technol. **1**, 135–150 (2012).
37. C.-C. Chiu and Y.-C. Lee, "Excimer laser micromachining of aspheric microlens arrays based on optimal contour mask design and laser dragging method," Opt. Express **20**, 5922–5935 (2012).
38. S. Tanaka, M. Mohri, A. Okada, H. Fukushi, and M. Esashi, "Versatile wafer-level hermetic packaging technology using anodically-bondable LTCC wafer with compliant porous gold bumps spontaneously formed in wet-etched cavities," in *IEEE 25th International Conference on Micro Electro Mechanical Systems (MEMS)* (IIEEE, 2012), pp. 369–372.
39. M. Wiemer, J. Frömel, C. Jia, S. Bargiel, M. Baranski, N. Passilly, and C. Gorecki, "Bonding and contacting of vertically integrated 3-D microscanners," in *IWLPC (Wafer-Level Packaging)* (Surface Mount Technology Association, 2012).
40. H. Tilmans, J. De Coster, P. Helin, V. Cherman, A. Jourdain, P. De Moor, B. Vandevelde, N. Pham, J. Zekry, A. Witvrouw, and I. De Wolf, "MEMS packaging and reliability: an undividable couple," Microelectron. Reliab. **52**, 2228–2234 (2012).
41. S. Bargiel, C. Jia, M. Baranski, J. Frömel, N. Passilly, C. Gorecki, and M. Wiemer, "Vertical integration technologies for optical transmissive 3-D microscanner based on glass microlenses," Procedia Eng. **47**, 1133–1136 (2012).
42. M. Wiemer, D. Wuensch, J. Frömel, T. Gessner, S. Bargiel, M. Baranski, and N. Passilly, "Multi-wafer bonding, stacking and interconnecting of integrated 3-D MEMS micro scanners," Int. J. Microwave Opt. Technol. **9**, 128–133 (2014).
43. S. Bargiel, C. Gorecki, M. Baranski, N. Passilly, M. Wiemer, C. Jia, and J. Frömel, "3D micro-optical lens scanner made by multi-wafer bonding technology," Proc. SPIE **8616**, 861605 (2013).
44. K. P. Larsen, J. T. Ravnkilde, and O. Hansen, "Investigations of the isotropic etch of an ICP source for silicon microlens mold fabrication," J. Micromech. Microeng. **15**, 873–882 (2005).
45. A. Laliotis, M. Trupke, J. Cotter, and G. Lewis, "ICP polishing of silicon for high quality optical resonators on a chip," J. Micromech. Microeng. **22**, 125011 (2012).